

Article

# High-Temperature Deformability of a Fe-Cr-Mn-Ni Austenite Stainless Steel with High Nitrogen and High Carbon Contents

Byung Ju Lee, Jae Sook Song and Sun Ig Hong \* 

Department of Advanced Materials Engineering, Chungnam National University, Daejeon 305-764, Korea; enll1234@naver.com (B.J.L.); jsongdoctor@yahoo.co.kr (J.S.S.)

\* Correspondence: sihong@cnu.ac.kr; Tel.: +82-42-821-6595 or +82-10-8803-6595

Received: 3 July 2018; Accepted: 31 July 2018; Published: 4 August 2018



**Abstract:** High temperature deformability and fracture behavior of deformation-processed high nitrogen high carbon Fe-Cr-Mn-Ni stainless steel rods were studied. The effective fracture elongation increased rapidly from 1000 °C, and reached high values (>45%) at 1100–1200 °C, accompanied by strain softening and stress serrations, supporting periodic dynamic recrystallization (DRX). Dynamically recrystallized grains were observed close to the fracture surface, suggesting that active DRX worked until its fracture. Pre-deformation-annealing of Fe-Cr-Mn-Ni stainless steel rods at 1200 °C was found to deteriorate in deformability above 1000 °C, while it enhanced ductility below 950 °C. Pre-deformation annealing had a negative effect on the deformability above 1000 °C due to the reduction of driving forces for DRX, but it exhibited a beneficial effect on the ductility at lower temperatures because of the ease of slip in large-grained structures. The fracture surface at 1250 °C exhibited intergranular fractures due to partial melting at grain boundaries, supported by the thermodynamic calculation of the solidus temperature of Fe-Cr-Mn-Ni austenite stainless steel. In this study, effective fracture elongation, defined based on the assumption that the effective gage length decreases with straining, was found to be an accurate measure of hot deformability.

**Keywords:** deformability; dynamic recrystallization; effective elongation; fracture; Fe-Cr-Mn-Ni; stainless steel

## 1. Introduction

Development of high-nitrogen high-manganese stainless steels containing no or little nickel have been driven by high and unstable nickel prices [1]. At a time of price increase and price volatility of nickel, nitrogen has been considered as a substitute for nickel [1]. The substitution of Ni with Mn and nitrogen has been proven to be successful in the production of austenitic stainless steels. In addition to stabilizing austenitic structures, nitrogen is known to reduce the stacking fault energy of austenitic stainless steels, resulting in a number of beneficial effects such as enhanced strength, fatigue resistance, and impact and fracture resistances [1–5]. Since nickel is known to be an allergen, nickel-less and/or nickel-free stainless steels are expected to be favored, especially for biomedical applications [6]. High-nitrogen, high-carbon Fe-Cr-Mn-Ni stainless steels with high Cr contents are known to have thermal stability due to their high temperature oxidation and wear resistances [1,7]. The formation of Cr nitrides, however, is known to reduce fracture toughness and corrosion resistance at intermediate temperatures [7–9].

High-nitrogen high-carbon Fe-Cr-Mn-Ni stainless steel with 20–22% chromium and 3–4% nickel has an austenite matrix because austenite can be stabilized by the high nitrogen and high manganese contents. It is commonly used for engine valves, because it has a high temperature of mechanical

stability and excellent corrosion properties in the environment of hot exhaust gases. The demand for high-nitrogen high-carbon Fe-Cr-Mn-Ni austenite stainless steel as automobile components has been increasing. However, the inhomogeneous distribution of various alloying elements and phases is known to aggravate the toughness, hot deformability, and fatigue resistance of the material. Furthermore, because of its intrinsic high temperature strength required for high temperature applications, the deformability of Fe-Cr-Mn-Ni austenite stainless steel is insufficient for forming defect-free parts and products using conventional deformation processing [7,9].

The material loss associated with fatal cracks and flaws in high-nitrogen high-carbon Fe-Cr-Mn-Ni austenite stainless steel during formation is known to increase the manufacturing cost. Lack of data on hot deformability and phase stability during thermo-mechanical processing at high temperatures may have restricted the use of high-nitrogen high-carbon high chromium austenite stainless steels [7,10,11]. Another reason for the lack of data on the hot deformability of high temperature steels is due to the difficulty of obtaining the tensile ductility data above 1000 °C. Since hot deformation simulators that are usually used to determine the hot deformability have a problem with gripping the tensile specimens in the heating zone, compressive deformability, or reduction of area (RA), lack of elongation in case of tensile testing is used to determine the hot deformability. The reduction of the area may not predict the region of the high deformability as accurately as the effective elongation, because severe local necking may overestimate the deformability of the specimen. In this study, effective fracture elongation, defined on the assumption that the effective gage length decreases with straining, instead of compressive deformability or reduction of area, was used to measure the hot deformability more accurately.

The objectives of the present study were to investigate the hot deformability and fracture behaviors of high-nitrogen high-carbon Fe-Cr-Mn-Ni austenite stainless steel at high temperatures (600–1250 °C), and to explore the ways to enhance the deformability of high-nitrogen high-carbon high-chromium steels.

## 2. Materials and Methods

High-nitrogen (0.40 wt.%) high-carbon (0.51 wt.%) Fe-21.7 Cr-9.7 Mn-3.4 Ni stainless steel with the chemical composition as shown in Table 1 was cast, homogenization-annealed at 1080 °C for 4 h, and hot rolled and groove-rolled to 15 mm diameter rods with intermediate heat treatments at 900 °C. The nitrogen was alloyed by bottom nitrogen gas injection in this study [12]. The carbon and nitrogen contents were determined using a Leco C/S-844 and Leco O/N-836 determinator, (Leco, Saint Joseph, MI, USA) respectively. The thermodynamic calculations were performed by Thermo-Calc software using the TCS Steel Database TCFE7 (Thermo-Calc Software, Solna, Sweden) [7,13] to predict the stability of various phases at high temperatures.

**Table 1.** The chemical composition of stainless steel used in the present study (wt.%).

Element	C	N	Mn	Cr	Ni	V	Si	B
Composition	0.51	0.40	9.71	21.7	3.40	0.07	0.11	0.003

In order to study the influence of annealing on the deformability and mechanical strength, the microstructure of specimen before and after tensile testing was examined using an optical microscope (Olympus, Tokyo, Japan) and an JSM-7000F (JEOL, Tokyo, Japan) scanning electron microscope (SEM). For prolonged annealing at high temperatures, lumps of steel ingots and groove-rolled rods were heat-treated, and the specimens were taken for observation and testing, away from the external surface. X-ray diffraction (XRD) analyses were carried out for phase identification, using Cu K $\alpha$  radiation at 35 KV and 25 mA on a Rigaku D/MAX-2200 diffractometer (Rigaku, Tokyo, Japan). The XRD scan was carried out at 0.028 steps with a 15-s counting time. Transmission electron microscopy (TEM) samples taken from the as-rolled rods were prepared by grinding discs down to 100- $\mu$ m thicknesses, followed

by electropolishing at  $-30\text{ }^{\circ}\text{C}$ . TEM observations were carried out using a JEOL 200C microscope (JEOL, Tokyo, Japan) at 200 kV equipped with JED-2300T (JEOL, Tokyo, Japan) energy dispersive spectroscopy (EDS).

A tensile specimen with a diameter of 5 mm (Figure 1a) was placed in a vacuum chamber of the hot deformation simulator, with an induction coil of 50 mm length for heating the tensile specimen (Figure 1b). High temperature tensile testing was performed at temperatures between  $600\text{--}1250\text{ }^{\circ}\text{C}$  and a cross-head speed of 100 mm/s using a Fuji Denpa (Kogyo, Japan) hot deformation simulator under vacuum conditions, with argon gas as a cooling medium. The temperature was controlled with a tolerance of  $\pm 5\text{ K}$  using a thermocouple. In order to examine the effect of high temperature annealing on the hot deformability, some of the specimens were machined from the groove-rolled rods that were annealed at  $1200\text{ }^{\circ}\text{C}$  for 7 h and 24 h. The average grain size increased to  $68.2 \pm 12.6\text{ }\mu\text{m}$  and  $123.6 \pm 21.3\text{ }\mu\text{m}$  after annealing at  $1200\text{ }^{\circ}\text{C}$  for 7 h and 24 h, respectively, from the initial grain size of  $15.3 \pm 2.8\text{ }\mu\text{m}$  in the groove-rolled steel. The tensile specimens were cooled rapidly by argon gas, and the surface and cross sections of fractured samples were also observed using OM and SEM.

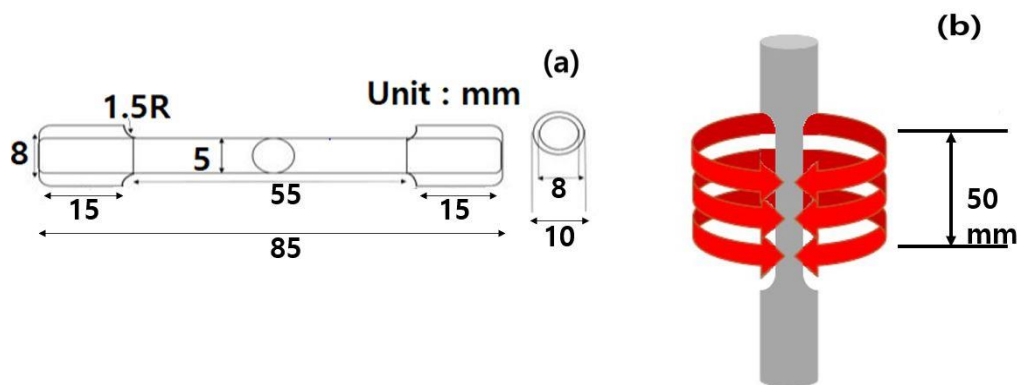


**Figure 1.** Tensile specimen with a diameter of 5 mm (a) placed in a vacuum chamber with an induction coil of 50 mm length for heating the tensile specimen (b).

### 3. Result and Discussion

#### 3.1. Thermodynamic Prediction of Phases and Their Stability

Hot cracking has been considered to be a serious problem in the high temperature formability of high-nitrogen high-carbon steels [9]. It has been reported that the surface and edge cracks of ingots during hot forging or hot rolling are caused by the precipitation of carbide/nitride and intermetallic phases [9]. The precipitation of  $\text{Cr}_2\text{N}$  has a detrimental effect on the formability of high-nitrogen steels [9]. The Thermo-Calc software was used to predict the existence and stability of phases, and to estimate the fraction of various phases with temperature. The effects of alloying elements in Fe-21.7 Cr-9.7 Mn-3.4 Ni with high carbon (0.51 wt.%) and nitrogen (0.40 wt.%) contents on the phase stability were also studied using Thermo-Calc software [13]. The effects of alloying elements other than carbon and nitrogen on the phase stability were found to be less pronounced in the composition range of interest.

In order to examine the effects of carbon or nitrogen addition on the stability of various phases, isopleth diagrams showing the stabilities of phases in Fe-21.7 Cr-9.7 Mn-3.4 Ni stainless steel as a function of carbon (a) or nitrogen content (b) are displayed in Figure 2a,b. In these phase diagrams, ferrite ( $\delta$ ), austenite ( $\gamma$ ),  $\text{Cr}_2\text{N}$ ,  $\text{M}_7\text{C}_3$ ,  $\sigma$ ,  $\text{M}_{23}\text{C}_6$ , and liquid phases are marked in the temperature-carbon (wt.%) or temperature-nitrogen (wt.%) space. In Figure 2, all other alloying elements were assumed to be the same, as shown in Table 1, except for carbon in Figure 2a or nitrogen in Figure 2b. The stabilities of  $\text{M}_{23}\text{C}_6$  and  $\text{Cr}_2\text{N}$  as a function of carbon (a) or nitrogen (b) in Figure 2 were of interest, because  $\text{M}_{23}\text{C}_6$  and  $\text{Cr}_2\text{N}$  can limit the deformability of Fe-21.7 Cr-9.7 Mn-3.4 Ni stainless steel. An interesting

observation in Figure 2b is that the high temperature stability of  $\text{Cr}_2\text{N}$  increased with an increase of nitrogen, up to 1.0 wt.% nitrogen. The stable carbide was found to be  $\text{M}_{23}\text{C}_6$ , and its high temperature stability increased with increasing carbon content, up to 0.6 wt.% carbon, as shown in Figure 2a. As the carbon content increased above 0.6 wt.%,  $\text{M}_7\text{C}_3$  carbides were found to be stable at high temperatures (>1100–1200 °C). The high temperature stability of  $\text{M}_{23}\text{C}_6$  carbides decreased with an increase of nitrogen content, as shown in Figure 2b. The addition of carbon was found to decrease the solidus temperature (Figure 2a), while the addition of nitrogen had little influence on the solidus temperature (Figure 2b).

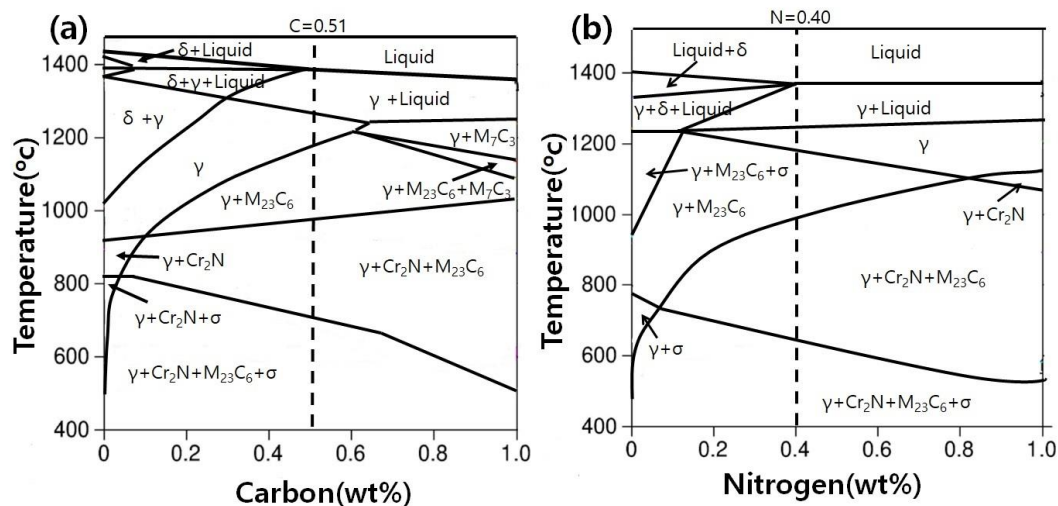


**Figure 2.** Isoleth diagrams showing the stability of phases such as ferrite, austenite,  $\text{Cr}_2\text{N}$ ,  $\text{M}_7\text{C}_3$ ,  $\sigma$ ,  $\text{M}_{23}\text{C}_6$ , and liquid in Fe-Cr-Mn-Ni stainless steel, as functions of temperature and carbon (a), or nitrogen (b).

In Figure 3, the computed mass fraction vs temperature diagram, showing the temperature range and mass fraction of ferrite, austenite  $\gamma$ ,  $\text{Cr}_2\text{N}$ ,  $\text{M}_{23}\text{C}_6$ , and liquid phases, is presented for high-nitrogen high-carbon Fe-21.7 Cr-9.7 Mn-3.4 Ni steel. The deformability and fracture behavior of high-carbon high-nitrogen Fe-Cr-Mn-Ni steel in the present study could be analyzed using the data on the phase stability and mass fraction of each phase, as a function of temperature. The precipitation and presence of  $\text{M}_{23}\text{C}_6$  would increase the strength and high temperature creep resistance, but would decrease the deformability. The appearance of the  $\text{Cr}_2\text{N}$  and liquid phase are also known to deteriorate the high temperature deformability [7,9].  $\text{M}_{23}\text{C}_6$  and  $\text{Cr}_2\text{N}$  were found to be completely dissolved at 1170 °C and 1000 °C, respectively, for the Fe-21.7 Cr-9.7 Mn-3.4 Ni steel with 0.40 wt.% nitrogen and 0.51 wt.% carbon. As shown in Figure 3,  $\text{Cr}_2\text{N}$  was less stable at high temperatures and its mass fraction was much smaller than that of  $\text{M}_{23}\text{C}_6$ ; it may have less influence on the hot deformability than  $\text{M}_{23}\text{C}_6$  [14]. The mass fraction of  $\text{Cr}_2\text{N}$  at 800 °C (3%) in the high-nitrogen high-carbon stainless steel of the present study was smaller than that in carbon-free high nitrogen Fe-12.4 Mn-16.1 Cr-3.3 Mo steel (7.3%), as reported by Erisir et al. [7].

### 3.2. Microstructural Analyses

The microstructure of groove-rolled rods exhibited equi-axed grains and carbide particles, mostly at grain boundaries, as shown in Figure 4a. The average sizes of grain and carbides were found to be 15.3  $\mu\text{m}$  and 0.86  $\mu\text{m}$ , respectively. XRD patterns in Figure 4b exhibited peaks from face-centered cubic (FCC) austenite, and  $\gamma$  and  $\text{M}_{23}\text{C}_6$  carbides in high-nitrogen high-carbon Fe-Cr-Mn-Ni stainless steel. Figure 5a,b displays the TEM microstructure of groove-rolled high-carbon high-nitrogen Fe-Cr-Mn-Ni rods. In the region with less carbide particles, thin twin bands were observed. The population of

deformation twin bands is known to be associated with the stacking fault energy [15–20]. The addition of Cr and Ni in Fe-Mn steels [16] and Mn in Fe-Mn-Si steels [15,17,18] are known to raise the stacking fault energy. Ullrich et al. [16] noted that the stacking fault energy of Fe-16Cr-6Mn-9Ni austenite stainless steel was 26 mJ/m<sup>2</sup>, and observed the abundant twins. M<sub>23</sub>C<sub>6</sub> particles were observed to be precipitated dominantly at grain boundaries, as shown in Figures 4a and 5b in the present study. EDS spectra from the particles (marked as “C”) exhibited major Cr peaks with C peaks (Figure 5c), and those from the matrix (marked as “D”) exhibit major Fe peaks, with minor peaks originating from other alloying elements, supporting the presence of M<sub>23</sub>C<sub>6</sub> carbides, as confirmed by XRD. The presence of twin bands in Figure 5b was less clear in the region of numerous M<sub>23</sub>C<sub>6</sub> particles, suggesting that small carbide particles were barriers to twin band propagation.

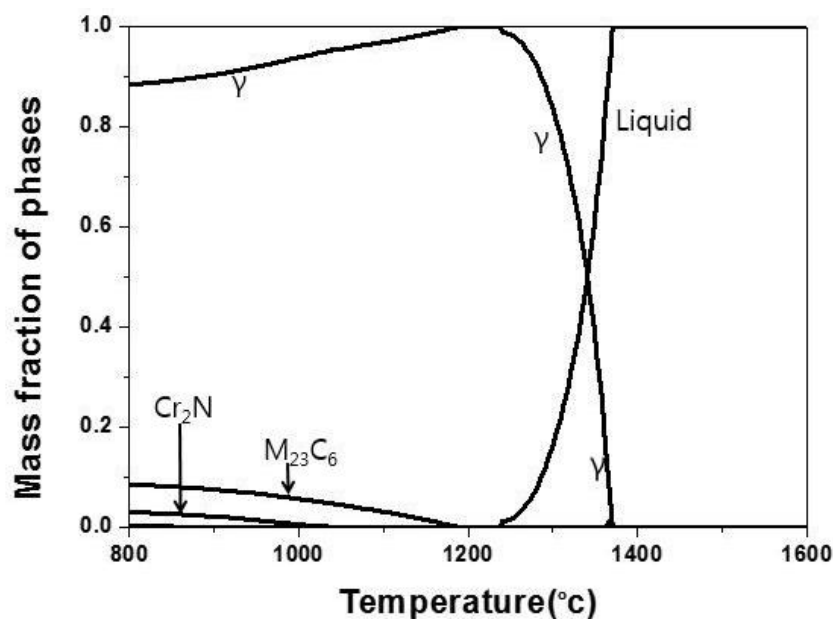


**Figure 3.** Computed mass fraction vs temperature diagram, showing the temperature range and mass fraction of ferrite, austenite  $\gamma$ , Cr<sub>2</sub>N, M<sub>23</sub>C<sub>6</sub>, and the liquid phase.

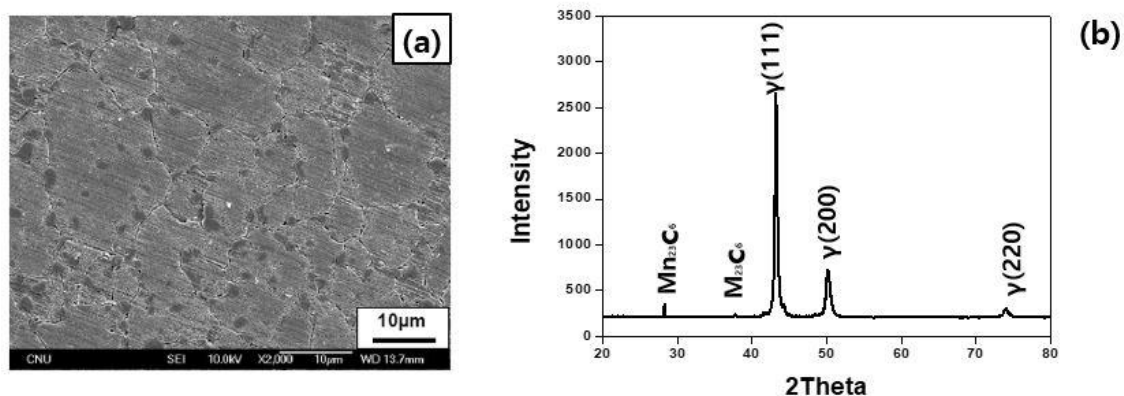


**Figure 4.** Microstructure (a) of groove-rolled rod, exhibiting equi-axed grains, and carbide particles, mostly at grain boundaries and XRD patterns (b) exhibiting the peaks from face-centered cubic (FCC) austenite and M<sub>23</sub>C<sub>6</sub> carbides.

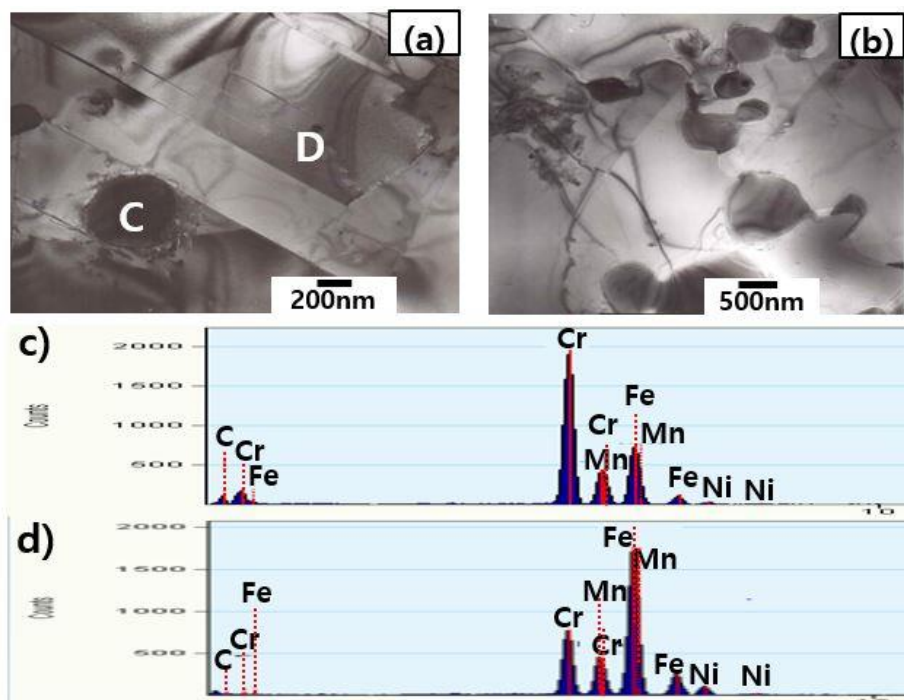


**Figure 5.** (a,b) Transmission electron microscopy (TEM) microstructures of groove-rolled high-carbon high-nitrogen Fe-Cr-Mn-Ni rods. Energy dispersive spectroscopy (EDS) spectra from the particles (c) and the matrix (d).

The  $\text{Cr}_2\text{N}$  phase was not easily observed in the groove-rolled high-nitrogen high-carbon Fe-Cr-Mn-Ni rod of the present study. In the as-cast ingot of high-carbon high-nitrogen Fe-Cr-Mn-Ni, extensive precipitation and growth of lamellar  $\text{Cr}_2\text{N}$  was observed at the grain boundaries in the temperature range of 800–900 °C [14]. Erisir et al. [7] also observed  $\text{Cr}_2\text{N}$  at grain boundaries in the high nitrogen (0.8 wt.%) as-cast Fe-Cr-Mn-Mo-Ni steel ingot. Vanderschaeve et al. [21] observed continuous precipitation in large-grain-sized (100–125  $\mu\text{m}$ ) high-nitrogen (0.9 wt.%) Cr-Mn steels at temperatures between 700–900 °C. In the groove-rolled Fe-Cr-Mn-Ni rod of the present study, as-cast ingots were homogenized at 1080 °C, at which the  $\text{Cr}_2\text{N}$  phase was fully dissolved into the  $\gamma$  matrix quickly because of the lower-volume fraction (3% at 800 °C) of  $\text{Cr}_2\text{N}$  (Figure 3), and instability at high temperatures. No elaborate efforts were made to identify the phases that were stable at lower temperatures, because the present work is focused on the effect of high temperature deformability.

### 3.3. High Temperature Stress-Strain Responses

The stress-stroke displacement curves of groove-rolled high-nitrogen high-carbon Fe-Cr-Mn-Ni austenite stainless steel of the present study are displayed in Figure 6. The strain cannot be defined unambiguously in the hot deformation simulator testing shown in Figure 1b. The upper and lower parts of the tensile specimen were elongated out of the heating coil during straining, decreasing the effective gage length of the specimen with the strain. This made accurate measurement of elongation impossible in the tensile testing using a hot deformation simulator [7,9] and no efforts were made to obtain the stress-strain curves from tensile testing using a hot deformation simulator. The effective gage length during deformation could be reasonably defined with the assumption that straining only occurred within the length of heating coil (50 mm), because the temperature of the upper and lower parts of the specimen that were elongated out of the heating coil would drop rapidly, and straining

outside of the heat coil would be negligible if there is any. The effective gage length of the specimen,  $L_{eff}$  can be defined as follows:

$$L_{eff} = L_o^2 / L_i = L_o^2 / (L_o + \Delta L) = L_o^2 / (L_o + s \cdot t) \quad (1)$$

where  $L_o$  is the initial gage length (length of heating coil (=50 mm)),  $L_i$  is the instantaneous gage length at the moment of the strain measurement,  $s$  is the stroke displacement rate, and  $t$  is the time. The increase of specimen length with time,  $\Delta L$  can be expressed as  $s \cdot t$ . Since the fraction of the gage length within the heating coil with straining can be expressed as  $L_o / (L_o + s \cdot t)$ , the effective gage length,  $L_{eff}$  can be determined as  $L_o^2 / (L_o + s \cdot t)$ . The effective strain can be obtained if the decrease of the effective gage length with straining is taken into consideration as follows:

$$\varepsilon_{eff} = \Delta L / L_{eff} = s \cdot t / L_{eff} = s \cdot t (L_o + s \cdot t) / L_o^2 = \Delta L (L_o + \Delta L) / L_o^2 \quad (2)$$

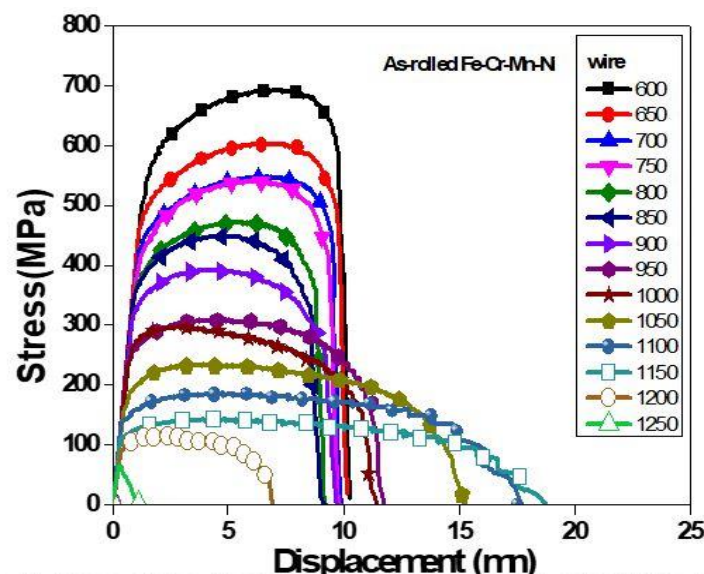


**Figure 6.** Stress-stroke displacement curves of groove-rolled high-carbon high-nitrogen Fe-Cr-Mn-N austenite stainless steel.

The effective stress-strain curves obtained using the effective strain defined above are displayed in Figure 7. The strength of the groove-rolled high-nitrogen high-manganese austenite stainless steel decreased with an increase in temperature. Stress-strain curves in Figure 7 show the decrease of the ultimate tensile strength (UTS) from 695 MPa to 103 MPa with an increase in temperature from 600 °C to 1200 °C. The stress-strain curves exhibited typical work hardening until the final stage of fracture, from 600 °C up to 900 °C. Above 950 °C, initial brief work hardening was followed by extended work softening. At temperatures below 1000 °C, the work hardening rate was controlled by the competition between generation and annihilation and dislocations [22]. It is interesting to note that the fracture elongation started to increase appreciably as the work softening became dominant in the stress-strain curves above 950 °C, suggesting the increase of ductility above 950 °C was associated with dynamic recovery and/or dynamic recrystallization. The critical strain at which the softening set in, decreased with an increase of temperature, which was consistent with the easier dynamic recrystallization with an increase of temperature [23,24].

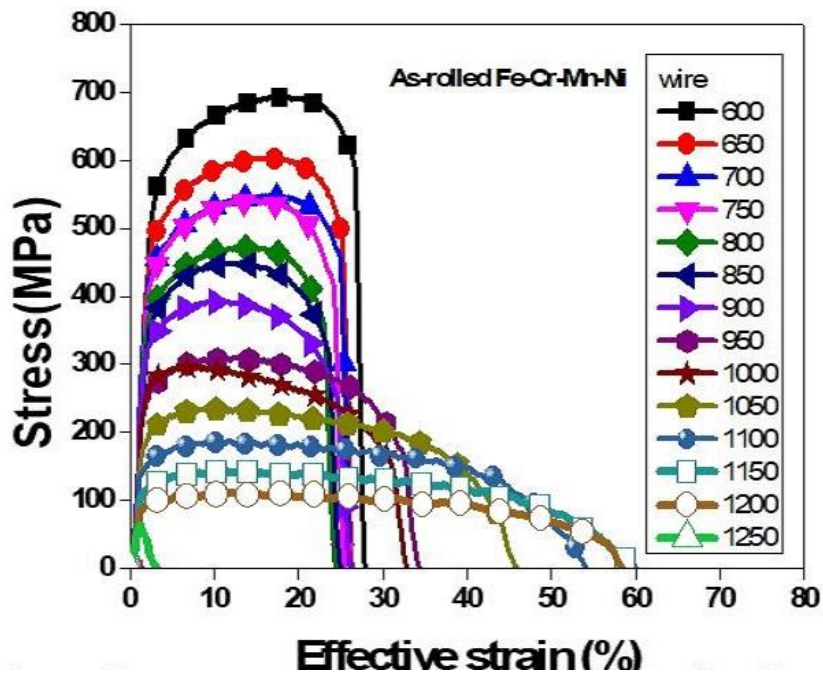


Figure 7. Effective stress-strain curves obtained using the effective strain defined in the present study.

The effective stress-strain curves of groove-rolled rods and those annealed at 1200 °C for 12 h and 24 h are displayed in Figure 8. The temperature at which the appreciable softening set in, after initial brief work hardening, increased from 950 °C to 1050 °C upon annealing at 1200 °C. The strength of high-nitrogen high-manganese austenite stainless steel decreased appreciably after annealing at 1200 °C for 12 h. The strength did not change much after further annealing up to 24 h, but the elongation-to-fracture decreased appreciably with annealing up to 24 h at 1200 °C.

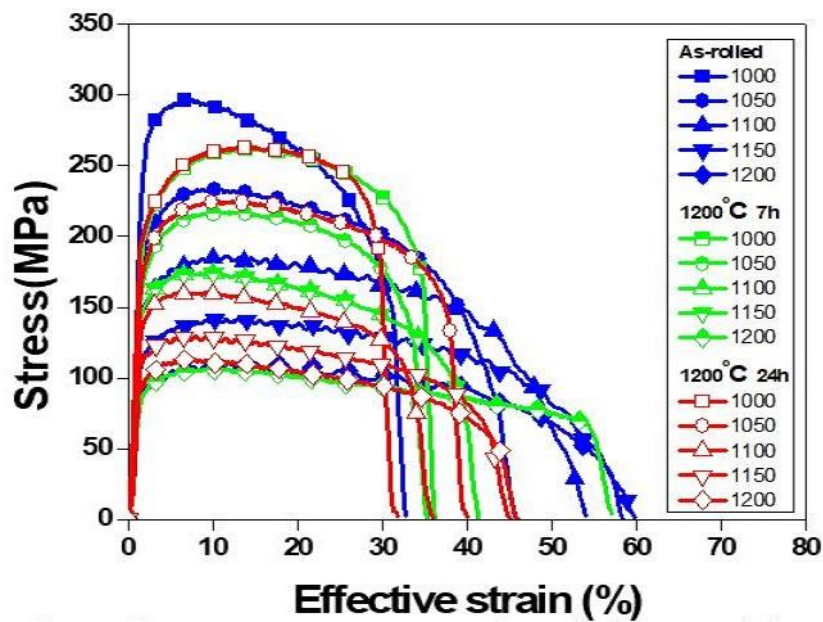
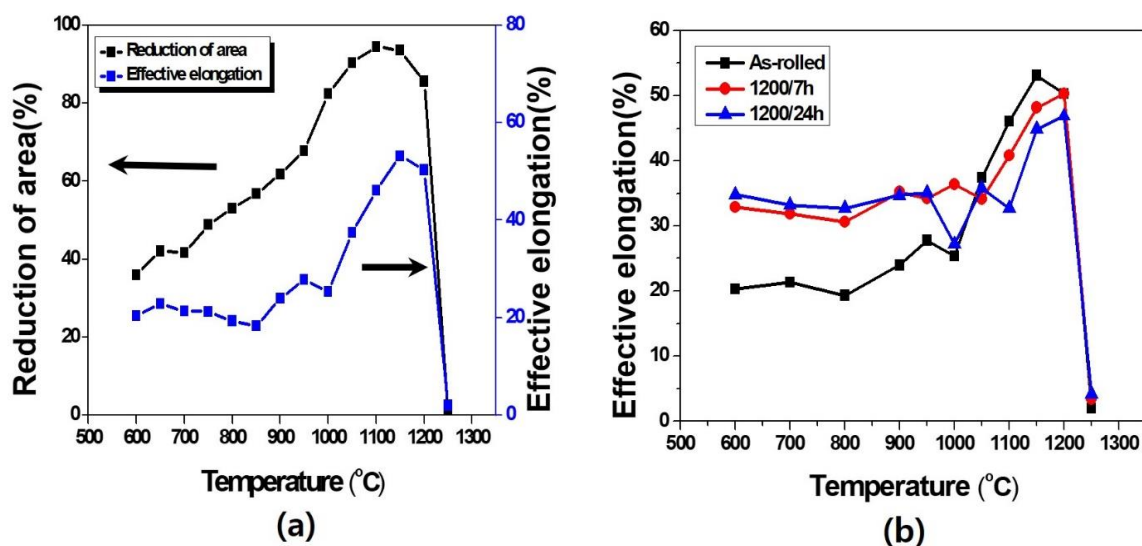


Figure 8. Effective stress-strain curves of as-rolled rods and those annealed at 1200 °C for 12 h and 24 h.

### 3.4. High Temperature Deformability and Fracture

Reduction of area has been used to measure the tensile hot deformability using a hot deformation simulator, since the fracture elongation cannot be accurately determined so far (Figure 1b). If the gage length is accurately defined, the fracture elongation can be considered as a more accurate measure of the deformability, because in some alloys with high reductions of area, premature fractures were observed to be associated with severely localized deformations in the necked region [25–28]. In the present study, the fracture elongation could be reasonably determined by introducing the concept of effective gage length that decreases with strain because the heated region of specimen decreases with strain (Figure 1b). The effective elongation-to-fracture obtained by Equation (2) is plotted along with the reduction of area as a function of temperature in Figure 9a. The reduction of area was measured accurately by measuring the fracture surface area in SEM micrographs, of the fractured specimens taken under the same conditions. In Figure 9a, the reduction of area increased gradually up to 950 °C, and then more rapidly up to 1100 °C. It decreased slightly at 1200 °C, and then plummeted to merely 1–2% at 1250 °C. It should be noted that the loss of strength as well as that of ductility occurred at 1250 °C.



**Figure 9.** (a) Effective elongation-to-fracture for as-rolled Fe-Cr-Mn-Ni stainless steel, plotted along with the reduction of area as a function of temperature. (b) Effective elongation-to-fracture for as-rolled Fe-Cr-Mn-Ni stainless steel and those annealed at 1200 °C, plotted as a function of temperature.

The effective fracture elongation did not change much up to 900 °C, but it increased rapidly from 1000 °C and reached high values, above 45%, at 1100–1200 °C. The slight decrease of fracture elongation at 850 °C may be attributed to the Cr<sub>2</sub>N precipitation in the temperature range of 800–900 °C [7,14,21]. The high temperature deformability of Fe-Cr-Mn-Ni stainless steel can be predicted satisfactorily by the effective fracture elongation, calculated using Equations (1) and (2). Hong et al. [25] observed that the increased reduction of area does not necessarily equate to increased ductility. The severely localized deformation in the neck was found to result in a ductility minimum in some alloys [25–28]. The reduction of area may not predict the region of the high deformability as accurately as the effective elongation [25,28], because severe local necking may overestimate the deformability of the specimen. In Figure 9, the temperature range with high enough deformability based on the effective elongation (>30% elongation) was 1030–1200 °C, which was smaller than the temperature range (850–1200 °C) estimated from the reduction of area (>60% RA). Strict control of the deformation processing temperature was required in order to decrease the material loss by forming defect-free and reliable Fe-Cr-Mn-Ni stainless steel parts in the temperature region of high

deformability. The effective fracture elongation defined in the present study was more reliable for predicting the deformation-processing temperature range with high hot deformability.

In Figure 9b, the effective fracture elongations for as-rolled Fe-Cr-Mn-Ni stainless steel and those annealed at 1200 °C are plotted as a function of temperature. It is interesting to note that the fracture elongation of Fe-Cr-Mn-Ni austenite stainless steel above 1000 °C decreased upon pre-deformation annealing at 1200 °C, as shown in Figure 9b. With increase of pre-deformation annealing time at 1200 °C, the high temperature deformability was aggravated. On the other hand, the fracture elongation increased appreciably below 950 °C with pre-deformation annealing at 1200 °C. The effect of pre-deformation annealing at 1200 °C apparently had a negative effect on the deformability above 1000 °C, but exhibited a beneficial effect at lower temperatures.

Figure 10 displays the fracture surfaces of Fe-Cr-Mn-Ni austenite stainless steel fractured at 850 °C (Figure 10a), 1000 °C (Figure 10b), 1100 °C (Figure 10c), 1150 °C (Figure 10d), 1200 °C (Figure 10e), and 1225 °C (Figure 10f). In Figure 9a, the reduction of area after fracture increased with temperature, and it reached a peak at 1100 °C. Up to 1200 °C, the fracture surfaces exhibited dimples, suggesting a ductile fracture. At 1225 °C, the fracture surface shows mostly ductile fractures, with a mixture of brittle fractures. The fracture surface of as-rolled Fe-Cr-Mn-Ni austenite stainless steel at 1250 °C, however, exhibited granular structures caused by premature partial melting at the grain boundaries. The partial melting at 1250 °C was supported by thermodynamic predictions in Figure 3 showing that the solidus temperature of Fe-Cr-Mn-Ni austenite stainless was 1230 °C.

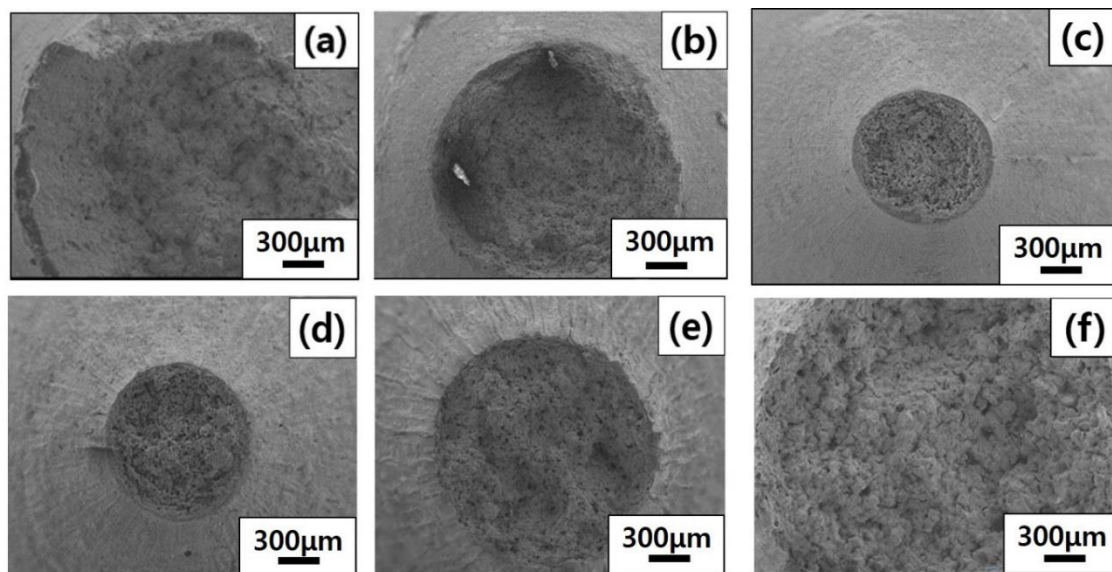


**Figure 10.** Fracture surfaces of Fe-Cr-Mn-Ni austenite stainless steel fractured at 850 °C (a), 1000 °C (b), 1100 °C (c), 1150 °C (d), 1200 °C (e), and 1225 °C (f).

### 3.5. Ductility Enhancement

The longitudinal cross sectional views of groove-rolled high-carbon high-nitrogen Fe-Cr-Mn-Ni steels fractured at various temperatures are exhibited in Figure 11. Near-fracture cross-sectional views at 850 °C exhibited string of small grains (2–4 μm) along the elongated grain boundaries, resulting in elongated necklace structures [29,30]. The appearance of small recrystallized grains in Figure 11a suggests that the critical strain for dynamic recrystallization (DRX) was attained at the final stage of fracture, and its contribution to ductility was minimal. At 1000 °C, the strings of small grains along the elongated grain boundaries increased appreciably, which may have contributed to the slight increase of ductility, as shown in Figure 9a. The temperature at which dynamic recrystallized grains were observed (>850 °C) in high carbon high nitrogen steel of the present study was lower than the temperature

for high-nitrogen low-carbon (0.033 wt.%) nickel-free stainless steel (>1050 °C) [7], and low-carbon (0.033 wt.%) high-nickel stainless steel (>1000 °C) [31,32]. The active dynamic recrystallization at lower temperatures in the present study was thought to be due to the lower melting temperature in the high-carbon high-nitrogen steel of the present study. The predicted melting temperature in Figure 2 was lower than that of high-nitrogen low-carbon (0.033 wt.%) nickel-free stainless steel [7] by 150 °C.

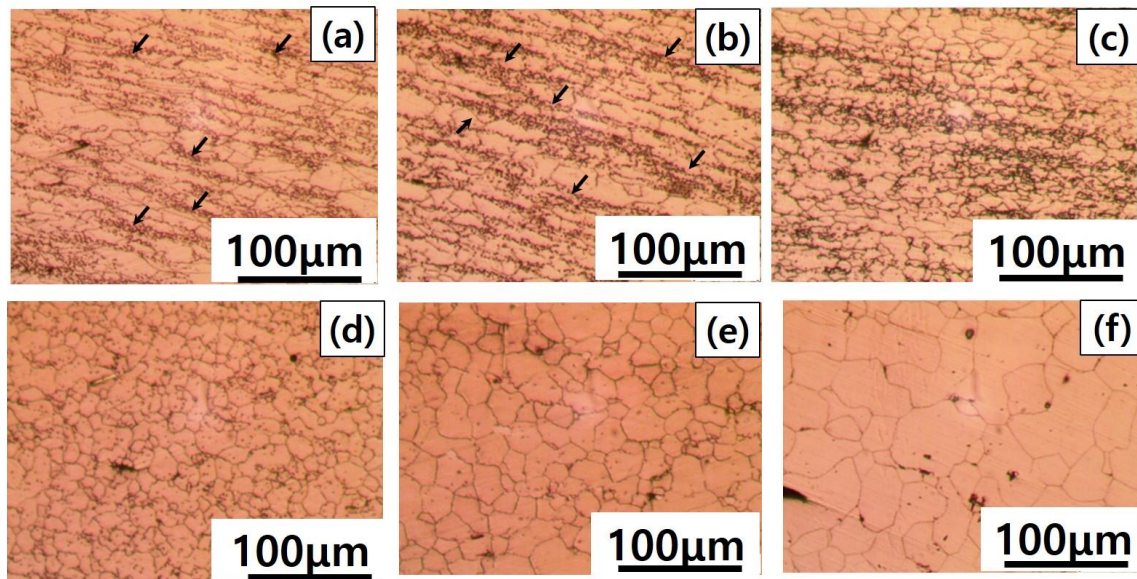


**Figure 11.** Longitudinal cross sectional views of groove-rolled high-carbon high-nitrogen Fe-Cr-Mn-Ni steels fractured at various temperatures; 850 °C (a), 1000 °C (b), 1100 °C (c), 1150 °C (d), 1200 °C (e), and 1225 °C (f).

At 1100 °C, dynamically recrystallized grains with some remains of necklace structures were visible, suggesting the presence of active dynamic recrystallization. The stress-strain response at 1100 °C in Figure 7 exhibited continuous softening initially after the peak stress, followed by serrated softening, suggesting periodic dynamic recrystallization (i.e., discontinuous dynamic recrystallization). At 1100 °C, more and more nuclei and newly recrystallized grains developed and, with further deformation, the recrystallized grains were deformed again, inducing periodic (discontinuous) dynamic recrystallization and enhanced ductility. This observation was consistent with the suggestion of Haghdadi et al. [33] that austenite stainless steel softens during hot deformation through discontinuous dynamic recrystallization, owing to its fairly low stacking fault energy [5]. The strain energy build-up is required before the activation of grain nucleation process. Serrations are thought to result from the repetition of the strain energy build up by dislocation build-up, and the strain energy release by recrystallization. At 1200 °C, the serration started from the beginning of plastic deformation, suggesting that the periodic dynamic recrystallization was dominant. The dynamically recrystallized grain size increased with an increase of temperature from 1100 °C to 1225 °C. It was obvious that the enhanced ductility at temperatures between 1000–1200 °C were associated with DRX. The grain boundary sliding suggested by Mirzaei et al. in an austenite stainless steel [32] could contribute to the enhanced ductility in the high-nitrogen high-carbon Fe-Cr-Mn-Ni stainless steel of the present study.

The longitudinal cross sectional views of as-rolled and annealed (1200 °C, 24 h) high-nitrogen, high-carbon Fe-Cr-Mn-Ni steels fractured at 1000 °C and 1100 °C are exhibited in Figure 12. At 1000 °C, the fracture elongation of annealed specimen was slightly larger or close to that of as-rolled specimens, as shown in Figure 9b. As explained, the strings of small grains along the elongated grain boundaries were observed for the as-rolled specimen fractured at 1000 °C (Figure 12a), suggesting that the dynamic

recrystallization (DRX) just started at the final stage of fracture, and its contribution to ductility was minimal. In the annealed (1200 °C, 24 h) steel fractured at 1000 °C, intersected and distorted slip lines were visible in the large-grained structure, with no sign of DRX, as shown in Figure 12c. At lower temperatures below 1000 °C, the ductility of annealed steel was greater than that of as-rolled steel, as shown in Figure 9b, because of ease of slip in the large-grained structures after annealing.

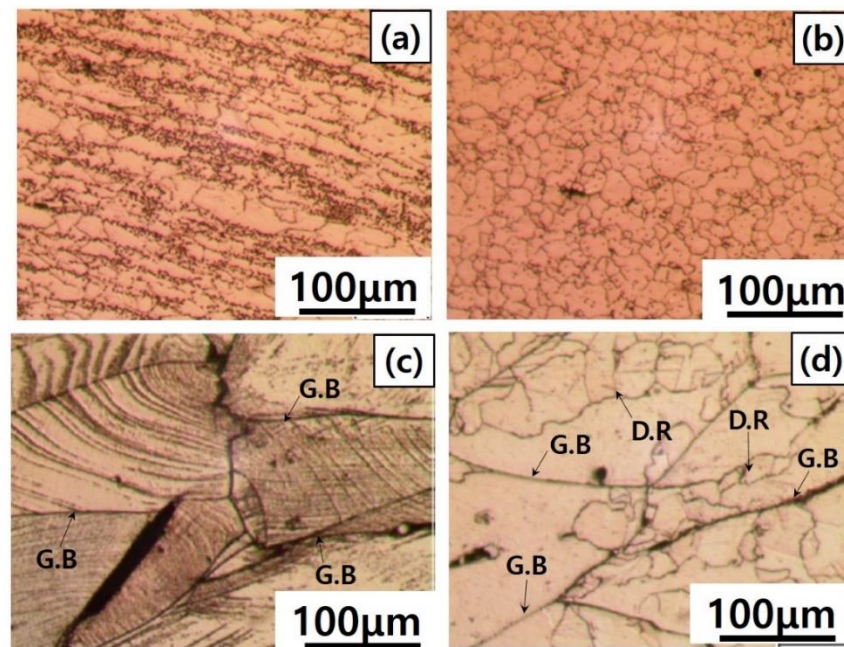


**Figure 12.** Longitudinal cross sectional views of as-rolled (a,b) and annealed (1200 °C, 24 h) (c,d) high-nitrogen, high-carbon Fe-Cr-Mn-Ni steels fractured at 1000 °C (a,c) and 1100 °C (b,d).

At 1100 °C, the fracture elongation of pre-deformation-annealed specimens is smaller than that of the as-rolled specimens. As stated above, stress-strain curves of the as-rolled specimens apparently exhibited stress serrations associated with periodic dynamic recrystallization at temperatures of 1100–1200 °C. After pre-deformation annealing at 1200 °C, however, stress serrations were barely observed. At 1100 °C, dynamically recrystallized grains were observed over the whole area in the as-rolled specimen as evidenced in Figure 12b. In the pre-deformation-annealed (1200 °C, 24 h) steel that was fractured at 1100 °C (Figure 12d), relatively large recrystallized grains were also observed at the initial grain boundaries (marked as G.B.), which were formed during annealing at 1200 °C. It should be noted that the microstructure shown in Figure 12d originated from the fractured specimen. The recrystallized grains (marked as D.R.) in Figure 12d grew larger in the pre-deformation-annealed (1200 °C, 24 h) steel at 1100 °C, since the driving force for the nucleation of recrystallized grain was much smaller, because of the release of cold work energy during pre-deformation annealing at 1200 °C.

#### 4. Conclusions

High temperature deformability and fracture behaviors of high-nitrogen high-carbon Fe-Cr-Mn-Ni austenite stainless steel were studied, and the conclusions are summarized as follows:

1. The stability of various phases in high nitrogen high carbon Fe-Cr-Mn-Ni steel was examined by thermodynamic modelling. The stable carbide was found to be  $M_{23}C_6$ , which is stable up to 1190 °C.
2. The effective elongation-to-fracture defined in this study was found to be a more accurate measure of the deformability than the reduction of area, because the premature fracture in some alloys is associated with the severe localization of deformation in the necked region.

3. The temperature range with high enough deformability based on the effective elongation (>30% elongation) was 1030–1200 °C, which is smaller than the temperature range (850–1200 °C) estimated from the reduction of area (>60% RA). The effective fracture elongation defined in the present study is more reliable in predicting the deformation-processing temperature range with high hot deformability.
4. The effective fracture elongation increased rapidly from 1000 °C and reached high values above 45% at 1100–1200 °C, accompanied by strain softening and stress serrations. Serrations are caused by the repetition of the strain energy build up by dislocation accumulation and strain energy release by recrystallization.
5. Pre-deformation annealing at 1200 °C aggravated the high temperature deformability to above 1000 °C, while it enhanced the ductility below 950 °C. Massive slip lines with no DRX were observed in annealed specimen deformed below 950 °C, resulting in enhanced ductility. Pre-deformation annealing aggravated deformability above 1000 °C by reducing the driving force for DRX.

**Author Contributions:** B.J.L. and J.S.S. designed and performed the experiments; S.I.H. analyzed the data and wrote the paper.

**Acknowledgments:** This research was supported by the Future Material Discovery Program of the National Research Foundation of Korea (NRF) funded by the Ministry of Science, ICT and Future Planning (MSIP) of Korea (2016M3D1A1023532) and High Value-Added Metallic Materials Specialist Training Program through the Korea Institute for Advancement of Technology (KIAT) funded by the Korea Ministry of Trade, Industry and Energy (G02P00720002001).

**Conflicts of Interest:** The authors declare no conflict of interest.

## References

1. Gavriljuk, V.G.; Berns, H. *High Nitrogen Steels*; Springer: Berlin, Germany, 1999.
2. Gu, J.; Li, J.; Chen, Y. Microstructure and Strengthening-Toughening Mechanism of Nitrogen-Alloyed 4Cr5Mo2V Hot-Working Die Steel. *Metals* **2017**, *7*, 310. [[CrossRef](#)]
3. Fava, A.; Montanari, R.; Richetta, M.; Varone, A. Analysis of Relaxation Processes in HNS Due to Interstitial-Substitutional Pairs. *Metals* **2017**, *7*, 246. [[CrossRef](#)]
4. Zhang, Y.; Li, J.; Shi, C.; Qi, Y.; Zhu, Q. Effect of Heat Treatment on the Microstructure and Mechanical Properties of Nitrogen-Alloyed High-Mn Austenitic Hot Work Die Steel. *Metals* **2017**, *7*, 94. [[CrossRef](#)]
5. Hong, S.I.; Laird, C. Mechanisms of slip mode modification in F.C.C. solid solutions. *Acta Metall. Mater.* **1990**, *38*, 1581–1594. [[CrossRef](#)]
6. Sumita, M.; Hanawa, T.; Teoh, S.H. Development of nitrogen-containing nickel-free austenitic stainless steels for metallic biomaterials—Review. *Mater. Sci. Eng. C* **2004**, *24*, 753–760. [[CrossRef](#)]
7. Erisir, E.; Prael, U.; Bleck, W. Hot deformation behavior and microstructural evolution of a nickel-free austenitic steel with high nitrogen content. *Metall. Mater. Trans. A* **2013**, *44*, 5549–5555. [[CrossRef](#)]
8. Menzel, J.; Kirschner, W.; Stein, G. High Nitrogen Containing Ni-free Austenitic Steels for Medical Applications. *ISIJ Int.* **1996**, *36*, 893–900. [[CrossRef](#)]
9. Erisir, E.; Prael, U.; Bleck, W. Effect of precipitation on hot formability of high nitrogen steels. *Mater. Sci. Eng. A* **2010**, *528*, 519–525. [[CrossRef](#)]
10. Kaputkina, L.M.; Prokoshkina, V.G.; Kviat, O.V.; Dyja, H.; Siwka, J.; Wiedermann, J. Structure and properties of nitrogen steels under hot deformation. *J. Mater. Process. Technol.* **2002**, *125–126*, 188–192. [[CrossRef](#)]
11. Speidel, M.O. Nitrogen Containing Austenitic Stainless Steels. *Mater. Sci. Eng. Technol.* **2006**, *37*, 875–880.
12. Gaye, H.; Huin, D.; Riboud, P.V. Nitrogen alloying of carbon and stainless steels by gas injection. *Metall. Mater. Trans. B* **2000**, *31*, 905–912. [[CrossRef](#)]
13. Shi, P.; Sundman, B. *Thermo-Calc TCC Software User' Guide*; Thermo-Calc Software AB: Stockholm, Sweden, 2008.
14. Oh, H.K.; Kim, I.W.; Park, S.M.; Hong, S.I. Stress-Strain Curves and Crack Formation in an Ingot of Stainless Steel 21-4N under High-Temperature Compression. *Met. Sci Heat Treat.* **2017**, *59*, 24–29. [[CrossRef](#)]

15. Ko, J.Y.; Hong, S.I. Microstructural evolution and mechanical performance of carbon-containing CoCrFeMnNi-C high entropy alloys. *J. Alloy. Compd.* **2018**, *743*, 115–125. [[CrossRef](#)]
16. Lu, J.; Hultman, L.; Holmstrom, E.; Antonsson, K.H.; Grehk, M.; Li, W.; Vitos, L.; Golpayegani, A. Stacking fault energies in austenitic stainless steels. *Acta Mater.* **2016**, *111*, 39–46. [[CrossRef](#)]
17. Pierce, D.T.; Jiménez, J.A.; Bentley, J.; Raabe, D.; Oskay, C.; Wittig, J.E. The influence of manganese content on the stacking fault and austenite/ $\epsilon$ -martensite interfacial energies in Fe–Mn–(Al–Si) steels investigated by experiment and theory. *Acta Mater.* **2014**, *68*, 238–253. [[CrossRef](#)]
18. Xiong, R.; Peng, H.; Si, H.; Zhang, W.; Wen, Y. Thermodynamic calculation of stacking fault energy of the Fe–Mn–Si–C high manganese steels. *Mater. Sci. Eng. A* **2014**, *598*, 376–386. [[CrossRef](#)]
19. Ullrich, C.; Eckner, R.; Krüger, L.; Martin, S.; Klemm, V.; Rafaja, D. Interplay of microstructure defects in austenitic steel with medium stacking fault energy. *Mater. Sci. Eng. A* **2016**, *649*, 390–399. [[CrossRef](#)]
20. Hong, S.I. Criteria for predicting twin-induced plasticity in solid solution copper alloys. *Mater. Sci. Eng. A* **2018**, *711*, 492–497. [[CrossRef](#)]
21. Vanderschaeve, F.; Taillard, R.; Foct, J. Discontinuous precipitation of Cr<sub>2</sub>N in a high nitrogen, chromium-manganese austenitic stainless steel. *J. Mater. Sci.* **1995**, *30*, 6035–6046. [[CrossRef](#)]
22. Hong, S.I.; Gray, G.T.; Lewandowski, J.J. Dynamic deformation behavior of Al–Zn–Mg–Cu alloy matrix composites reinforced with 20 Vol.% SiC. *Acta Metall. Mater.* **1993**, *41*, 2337–2351. [[CrossRef](#)]
23. Sakthivel, I.; Vasudevan, M.; Laha, K.; Parameswaran, P.; Chandravathi, K.S.; Panneer Selvi, S.; Maduraimuthu, V.; Mathew, M.D. Creep rupture behavior of 9Cr–1.8W–0.5Mo–VNb (ASME grade 92) ferritic steel weld joint. *Mater. Sci. Eng. A* **2014**, *591*, 111–120. [[CrossRef](#)]
24. Wu, C.; Cai, M.; Yang, P.; Su, J.; Guo, X. Physically-Based Modeling and Characterization of Hot Flow Behavior in an Interphase-Precipitated Ti–Mo Microalloyed Steel. *Metals* **2018**, *8*, 243. [[CrossRef](#)]
25. Hong, S.I.; Ryu, W.S.; Rim, C.S. Thermally activated deformation of Zircaloy-4. *J. Nucl. Mater.* **1984**, *120*, 1–5. [[CrossRef](#)]
26. Ha, J.S.; Hong, S.I. Deformation and fracture of Ti/439 stainless steel-clad composite at intermediate temperatures. *Mater. Sci. Eng. A* **2016**, *651*, 805–809. [[CrossRef](#)]
27. Hong, S.I. Influence of dynamic strain aging on the dislocation substructure in a uniaxial tension test. *Mater. Sci. Eng.* **1986**, *79*, 1–7. [[CrossRef](#)]
28. Conrad, H. Effect of interstitial solutes on the strength and ductility of titanium. *Prog. Mater. Sci.* **1981**, *26*, 123–403. [[CrossRef](#)]
29. Quan, G.Z. Characterization for Dynamic Recrystallization Kinetics Based on Stress–Strain Curves. In *Recent Development in the study of Recrystallization*; Wilson, P., Ed.; InTech: Rijeka, Croatia, 2013.
30. Jafari, M.; Najafizadeh, A. Correlation between Zener–Hollomon parameter and necklace DRX during hot deformation of 316 stainless steel. *Mater. Sci. Eng. A* **2009**, *501*, 16–25. [[CrossRef](#)]
31. Mirzaei, A.; Hanzaki, Z.; Haghdadi, N.; Mirzaei, A. Constitutive description of high temperature flow behavior of Sanicro-28 super-austenitic stainless steel. *Mater. Sci. Eng. A* **2014**, *589*, 76–82. [[CrossRef](#)]
32. Mirzaei, A.; Hanzaki-Zarei, A.; Abedi, H.R. Hot Ductility Characterization of Sanicro-28 Super-Austenitic Stainless-Steel. *Metall. Mater. Trans. A* **2016**, *47*, 2037–2048. [[CrossRef](#)]
33. Haghdadi, N.; Cizek, P.; Beladi, H.; Hodgson, P.D. The austenite microstructure evolution in a duplex stainless steel subjected to hot deformation. *Phil. Mag.* **2017**, *97*, 1209–1237. [[CrossRef](#)]

